Fig. 7. Light micrographs of paraffin sections of mouse thymic tissues at 3 (**a, b**), 10 (**c, d**) and 30 sec (**e, f**) after QD injections via left ventricles, prepared with IVCT. Both hematoxylin-eosin staining (HE; **a, c, e**) and red fluorescence signals (UV; **b, d, f**) emitted by ultraviolet wavelength were checked in serial tissue sections. (**a, b**) At 3 sec, QDs are slightly detected in small numbers of thick blood vessels (arrowheads) in corticomedullary boundary areas, but not in other blood vessels (arrows), including blood capillaries. (**c, d**) At 10 sec, they are more widely detected in the blood vessels in corticomedullary boundary areas (arrowheads), but are not yet seen in blood capillaries (arrows). (**e, f**) At 30 sec, they are seen in all the thick blood vessels (arrowheads), including blood capillaries (arrows), of the thymic tissues. Co, cortex. M, medulla. Bars=50 μm; inset, 100 μm.

Table 4. *Semi-quantitative comparison of relative QD localizations, as shown in Figure 7, in blood vessels of different areas of thymic tissues after QD injection on paraffin-embedded sections*

		Time intervals after QD injection via left ventricles		
		3 s	10 s	30 s
Blood vessels (15–30 μm) in corticomedullary boundary areas	Inside of vessels	+	++	+++
	Interstitium around vessels	–	–	–
Blood capillaries (~10 μm) in outer cortical areas	Inside of capillaries	–	+	++
	Interstitium around capillaries	–	–	–

(+++) Strongly positive. (++) Moderately positive. (+) Slightly positive. (–) Negative.
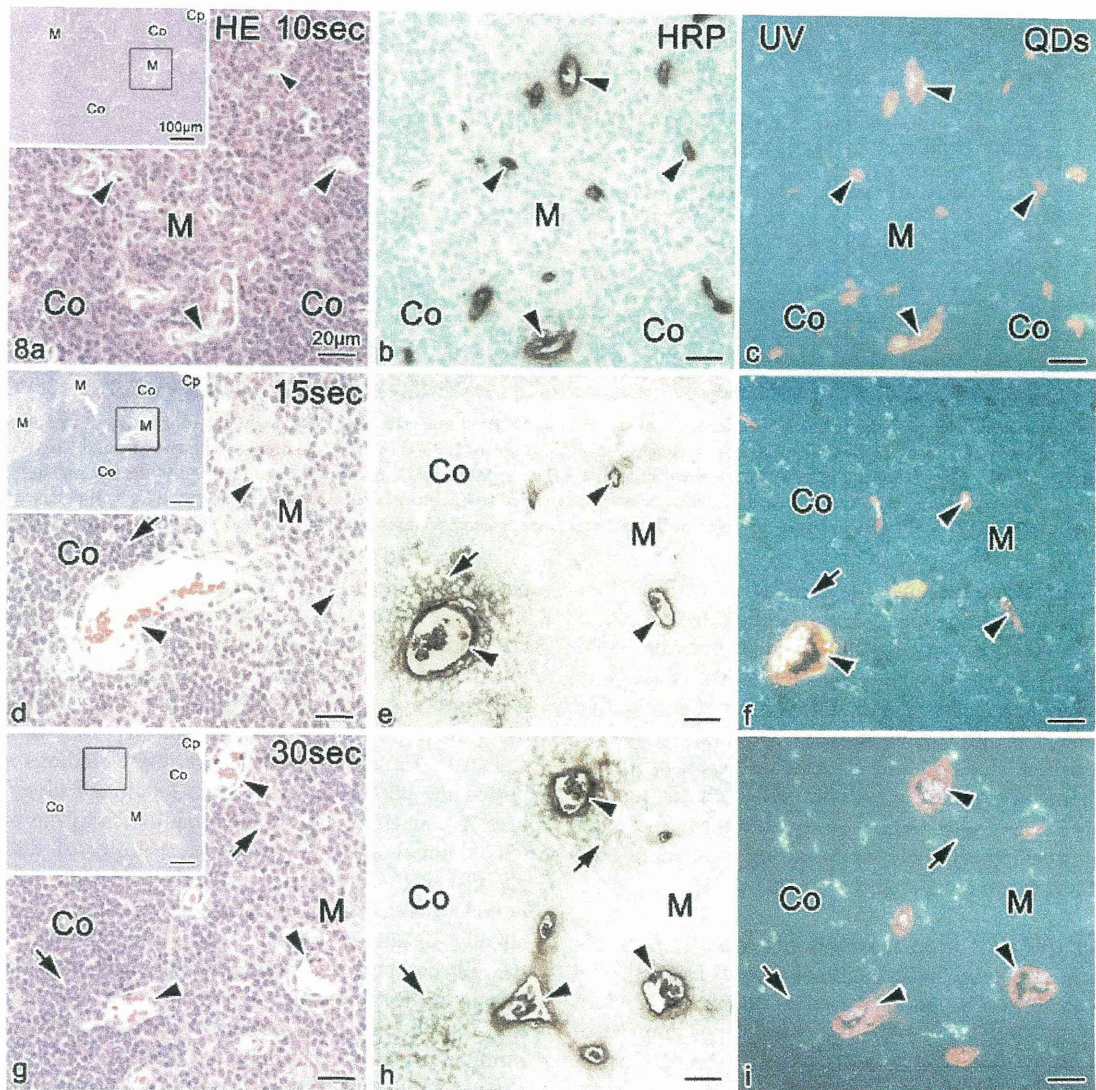
Fig. 8. Light micrographs of colocalization of QDs and HRP in serial paraffin sections by fluorescence or light microscopy. At 10 sec after the mixed QD and HRP injection, both are seen in blood vessels (arrowheads in **b**, **c**). At 15–30 sec, HRP has definitely leaked out into the interstitium around some thick blood vessels in the corticomedullary boundary areas (arrows in **e**, **h**), not in the cortex, but the QDs are still localized in blood vessels (arrowheads in **f**, **i**). Co: cortex. M: medulla. **a**, **d**, **g**: HE staining. **b**, **e**, **h**: immunostaining for HRP. **c**, **f**, **i**: fluorescent QDs. Bars=20 μm.

DAPI staining (Fig. 9c). The red fluorescence signals of Iba1 were mainly detected in the cytoplasm of macrophages, and HRP immunostaining was also seen in macrophages (Fig. 9c, double arrowheads). HRP immunofluorescence was still detected in blood vessels 30 min after HRP injection (Fig. 9a, c, arrowheads), in addition to some local interstitial areas (Fig. 9a, c, arrows).

IV. Discussion

Merits of IVCT for demonstration of HRP

The main feature of IVCT presented in this study was to obtain tissue specimens of living animal organs, which can strictly capture their dynamic circulation states including cells and tissues, as already discussed in detail [27]. It

is well known that conventional immunohistochemical techniques have some problems with molecular diffusion artifacts and antigen masking for the detection of soluble components in living animal organs. In contrast, the IVCT has various technical merits, including the prevention of tissue shrinkage or diffusion artifacts, a natural antigen-retrieval effect, and time-dependent analyses in the order of seconds. Therefore, it has been often used to analyze the immunolocalization of soluble proteins in cells and tissues of living animal organs under various hemodynamic conditions [27]. As compared with previous studies of molecular movement in the thymic interstitium for immunology, such as antigen presentation in functional thymic tissues [17], the present study showed small molecular HRP with dose- and time-dependent leakage through different thymic blood
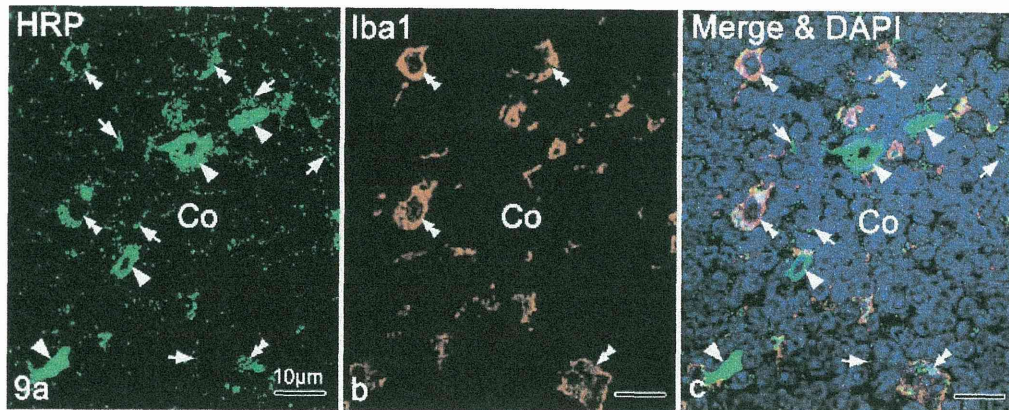
Fig. 9.   Immunofluorescence micrographs of cryosections of thymic cortical areas at 30 min after HRP (100 mg/ml) injection via left ventricles of living mice, prepared by IVCT. Double-immunofluorescence staining for HRP (a, c, green) and ionized calcium-binding adapter molecule 1 (Iba1) (b, c, red) with nuclear DAPI staining (blue) show their colocalization in almost all macrophages. Iba1 immunofluorescence shows the macrophages of thymic tissues (b, c, double arrowheads), which contain HRP in their cytoplasm (a, c, double arrowheads). HRP immunostaining is still detected within the blood vessels (a, c, arrowheads) and some areas of the cortical interstitium among compact thymocytes (a, c, arrows). Co, cortex. Bars=10 μm.

vessels, because of the high time-resolution of IVCT for dynamic functional structures [36]. Although the IVCT is a cryofixation method, which is not designed for time-lapse imaging, the present study also indicates that it is useful to examine the dynamically changing flux of extrinsic soluble HRP proteins in the thymic tissues. The IVCT was also found to be used for both enzyme-histochemical or immunohistochemical studies of soluble HRP circulation, as shown in Figures 3–5, and would be helpful for other enzyme-histochemical analyses due to the remaining high sensitivity of cryofixed enzyme reactions.

Permeability of HRP or BSA through different blood vessels

It is well known that the animal thymus has a special vascular complex, conventionally termed the blood–thymus barrier [3, 7, 15, 17, 29, 30], as an initial exposure site of lymphocytes to circulating antigens. The blood–thymus barrier has been assumed to be a reliable structure in the anatomical and functional sense, but foreign antigens can probably permeate its barrier under certain conditions. It has been also reported to consist of capillary endothelial cells, basal lamina of endothelium, perivascular spaces, basal lamina of epithelial reticulum cells and finally epithelial reticulum cells themselves. A previous experiment using ultrastructural tracers of different molecular weights demonstrated that immunological lymphoid cells in the thymic cortex were usually protected from circulating antigenic molecules in contrast with those of the medulla [29]. The interstitial tissues with augmented permeability of antigen proteins under some conditions *in vivo* would increase the accessibility of thymocytes to blood-derived molecules. However, based on the experiment with BSA of various concentrations, as performed previously using the living mouse thymic tissues [3], we found that the injected BSA was time-dependently distributed throughout the thymic interstitium in hours to days, leaking from thick blood vessels at the corticomedullary boundary, but not from

blood capillaries in outer cortical areas. In the present study, we have also revealed the similar localization of HRP protein in the thymic interstitium of living mice in a few minutes, indicating the easy leakage of small molecular HRP into corticomedullary boundary areas, depending on the time after HRP injection and its concentration, as shown in Figures 3–5. Therefore, these findings also supported the partial existence of a functional blood–thymus barrier, especially along blood capillaries of the outer cortex, although the molecular permeability of thick blood vessels, including some arterioles, in corticomedullary boundary areas was higher than that in the outer cortex, as already discussed [4, 15, 30]. In contrast, the thymic medulla contains leaky blood vessels, namely postcapillary venules. The time- and concentration-dependent localization of antigenic HRP proteins might be helpful for other immunohistochemical analyses of native thymic structures tissues with various interstitial fluid pressures and also determination of the immunological system *in vivo*.

Different states of blood-thymus barriers

In the case of QD injection with a high molecular complex, we did not find leakage of QD probes through any blood vessels of thymic tissues in the order of seconds, as shown in Figures 7 and 8. Our findings definitely showed the blood flow route from thick arterioles at the corticomedullary boundary at 3 sec, and then to thin blood capillaries in the inner cortex, as schematically summarized in Figure 2b. In addition, other reports have already demonstrated that transudation into thymic interstitial matrices depended on the molecular weight of the administered substances [4, 7, 13, 16, 17, 23, 29, 31]. The distribution of injected HRP of low molecular weight presented in this study seems to be additionally related to the vascular structures in the thymic cortex, because larger intrinsic IgA and IgM immunostaining intensities were less detected in the outer cortex in comparison with both extrinsic BSA and

mouse original albumin. as already discussed [3]. Therefore. it is concluded that an incomplete blood–thymus barrier in the corticomedullary boundary areas usually contributes to such different morphofunctional data of thymic tissues of living mice. which was directly revealed by IVCT-FS. probably reflecting their living state.

Demonstration of native blood flow routes

In addition. rapid QD distribution in the order of seconds was also visualized in the living mouse thymus with IVCT-FS. reflecting the *in vivo* blood flow condition. as reported previously [36]. Following the scheme of blood vessels (Fig. 2b). they formed branching and anastomosing loops in outermost regions of the cortical area. At the junction of the cortex and medulla. arterioles usually run upward to the surface capsule. continuing into blood capillaries within a short distance under the capsule. and then blood capillaries return as postcapillary venules to medullary thick veins (Fig. 2b). In corticomedullary boundary areas. arteries branch into arterioles. from which anastomosing blood capillaries break off into the inner cortex. As shown in Figures 7 and 8. QDs flowing in blood vessels did not leak out into the interstitium of thymic tissues in the order of seconds. indicating no transudation of QDs of larger molecular size. as discussed previously [36].

Phagocytosis of leaked HRP into macrophages

In the thymus. as shown in Figure 9. macrophages around the blood vessels actively phagocytized the permeated HRP. The permeability of the vessels in the thymus is known to be relatively low. as compared with that of blood vessels in other lymphatic tissues. Four subpopulations of mouse thymic macrophages have already been identified. including dendritic macrophages. plate-shaped macrophages. small oval macrophages. and ED1+-thymic macrophages [20]. Each subpopulation has different functions in the outer or inner cortex and the medulla. The HRP immunostaining intensity later decreased in the interstitium of the thymic cortex in comparison with the inside of blood vessels. as shown in Figures 3m and 5m. Such phagocytotic functions of macrophages within 30 min might change the average molecular concentrations of HRP in the thymic interstitium. depending on the time course of flowing HRP molecules. Moreover. the phagocytosis of HRP into macrophages could induce their expression of specific antigens. probably resulting in the common positive or negative immunoreaction pathway in other thymic cells. Therefore. in a future study. the IVCT will be additionally used to clarify T-cell differentiation at various sites of thymic tissues. probably depending on the dynamic diffusion of various serum components in their microenvironment. A further experiment at an electron microscopic level will be also necessary to directly examine the HRP penetration of blood vessels and phagocytotic macrophages of living mice. which could be prepared by IVCT.

VI. References

1. Bai. Y.. Ohno. N.. Terada. N.. Saitoh. S.. Nakazawa. T.. Nakamura. N.. Katoh. R. and Ohno. S. (2009) Immunolocalization of serum proteins in xenografted mouse model of human tumor cells by various cryotechniques. *Histol. Histopathol.* 24; 717–728.
2. Bai. Y.. Wu. B.. Terada. N.. Ohno. N.. Saitoh. S.. Saitoh. Y. and Ohno. S. (2011) Histological study and LYVE-1 immunolocalization of mouse mesenteric lymph nodes with "in vivo cryotechnique". *Acta Histochem. Cytochem.* 44; 81–90.
3. Bai. Y.. Wu. B.. Terada. N.. Saitoh. Y.. Ohno. N.. Saitoh. S. and Ohno. S. (2012) Immunohistochemical analysis of various serum proteins in living mouse thymus with "in vivo cryotechnique". *Med. Mol. Morphol.* 45; 129–139.
4. Drumea-Mirancea. M.. Wessels. J. T.. Müller. C. A.. Essl. M.. Eble. J. A.. Tolosa. E.. Koch. M.. Reinhardt. D. P.. Sixt. M.. Sorokin. L.. Stierhof. Y.. Schwarz. H. and Klein. G. (2006) Characterization of a conduit system containing laminin-5 in the human thymus: a potential transport system for small molecules. *J. Cell Sci.* 119; 1396–1405.
5. Elmore. S. A. (2006) Enhanced histopathology of the thymus. *Toxicol. Pathol.* 34; 656–665.
6. Graham. R. C. Jr. and Karnovsky. M. J. (1966) The early stages of absorption of injected horseradish peroxidase in the proximal tubules of mouse kidney: ultrastructural cytochemistry by a new technique. *J. Histochem. Cytochem.* 14; 291–302.
7. Green. I. and Bloch. K. (1963) Uptake of particulate matter within the thymus of adult and new-born mice. *Nature* 200; 1099–1101.
8. Henry. L.. Durrant. T. E. and Anderson. G. (1992) Pericapillary collagen in the human thymus: implications for the concept of the 'blood-thymus' barrier. *J. Anat.* 181; 39–46.
9. Hopwood. D. (1969) Fixatives and fixation: a review. *Histochem. J.* 1; 323–360.
10. Hopwood. D.. (1985) Cell and tissue fixation. 1972–1982. *Histochem. J.* 17; 389–442.
11. Ito. T. and Hoshino. T. (1966) Light and electron microscopic observations on the vascular pattern of the thymus of the mouse. *Arch. Histol. Jpn.* 27; 351–361.
12. Jin. T.. Fujii. F.. Komai. Y.. Seki. J.. Seiyama. A. and Yoshioka. Y. (2008) Preparation and characterization of highly fluorescent. glutathione-coated near infrared quantum dots for in vivo fluorescence imaging. *Int. J. Mol. Sci.* 9; 2044–2061.
13. Kato. S. (1997) Thymic microvascular system. *Microsc. Res. Tech.* 38; 287–299.
14. Kazuta. Y. (1994) An Atlas of the Experimental Animal Technology. Adthree Publishing Co. Ltd. Tokyo. Japan. p. 13.
15. Kendall. M. D. (1991) Functional anatomy of the thymic microenvironment. *J. Anat.* 177; 1–29.
16. Kyewski. B. A.. Fathman. C. and Kaplan. H. (1984) Intrathymic presentation of circulating non-major histocompatibility complex antigens. *Nature* 308; 196–199.
17. Kyewski. B. A.. Fathman. C. G. and Rouse. R. V. (1986) Intrathymic presentation of circulating non-MHC antigens by medullary dendritic cells: an antigen-dependent microenvironment for T cell differentiation. *J. Exp. Med.* 163; 231–246.

18. Ladi, E., Yin, X., Chtanova, T. and Robey, E. A. (2006) Thymic microenvironments for T cell differentiation and selection. *Nat. Immunol.* 7: 338–343

19. Lind, E. F., Prockop, S. E., Porritt, H. E. and Petrie, H. T. (2001) Mapping precursor movement through the postnatal thymus reveals specific microenvironments supporting defined stages of early lymphoid development. *J. Exp. Med.* 194: 127–134.

20. Liu, L. T., Lang, Z. F., Li, Y., Zhu, Y. J., Zhang, J. T., Guo, S. F., Wang, J. X., Wang, H. W. and Xu, Y. D. (2013) Composition and characteristics of distinct macrophage subpopulations in the mouse thymus. *Mol. Med. Rep.* 7: 1850–1854.

21. Marshall, A. H. and White, R. G. (1961) The immunological reactivity of the thymus. *Br. J. Exp. Pathol.* 42: 379–385.

22. Mason, D. Y. and Biberfeld, P. (1980) Technical aspects of lymphoma immunohistology. *J. Histochem. Cytochem.* 28: 731–745.

23. Müller, S. M., Stolt, C. C., Terszowski, G., Blum, C., Amagai, T., Kessaris, N., Iannarelli, P., Richardson, W. D., Wegner, M. and Rodewald, H. (2008) Neural crest origin of perivascular mesenchyme in the adult thymus. *J. Immunol.* 180: 5344–5351.

24. Ohno, N., Terada, N. and Ohno, S. (2006) Histochemical analyses of living mouse liver under different hemodynamic conditions by "in vivo cryotechnique." *Histochem. Cell Biol.* 126: 389–398.

25. Ohno, N., Terada, N., Bai, Y., Saitoh, S., Nakazawa, T., Nakamura, N., Naito, I., Fujii, Y., Katoh, R. and Ohno, S. (2008) Application of cryobiopsy to morphological and immunohistochemical analyses of xenografted human lung cancer tissues and functional blood vessels. *Cancer* 113: 1068–1079.

26. Ohno, S., Terada, N., Fujii, Y., Ueda, H. and Takayama, I. (1996) Dynamic structure of glomerular capillary loop as revealed by an in vivo cryotechnique. *Virchows Arch.* 427: 519–527.

27. Ohno, S., Terada, N., Ohno, N., Saitoh, S., Saitoh, Y. and Fujii, Y. (2010) Significance of 'in vivo cryotechnique' for morphofunctional analyses of living animal organs. *J. Electron Microsc.* 59: 395–408.

28. Pearse, G. (2006) Normal structure, function and histology of the thymus. *Toxicol. Pathol.* 34: 504–514.

29. Raviola, E. and Karnovsky, M. J. (1972) Evidence for a blood–thymus barrier using electron-opaque tracers. *J. Exp. Med.* 136: 466–498.

30. Roberts, R. L. and Sandra, A. (1994) Transport of transferrin across the blood-thymus barrier in young rats. *Tissue Cell* 26: 757–766.

31. Sainte-Marie, G. (1963) Antigen penetration into the thymus. *J. Immunol.* 91: 840–845.

32. Saitoh, S., Terada, N., Ohno, N. and Ohno, S. (2008) Distribution of immunoglobulin-producing cells in immunized mouse spleens revealed with "in vivo cryotechnique". *J. Immunol. Methods* 29: 114–126.

33. Shi, L., Terada, N., Saitoh, Y., Saitoh, S. and Ohno, S. (2011) Immunohistochemical distribution of serum proteins in living mouse heart with in vivo cryotechnique. *Acta Histochem. Cytochem.* 44: 61–72.

34. Shimo, S., Saitoh, S., Terada, N., Ohno, N., Saitoh, Y. and Ohno, S. (2010) Immunohistochemical detection of soluble immunoglobulins in living mouse small intestines using an in vivo cryotechnique. *J. Immunol. Methods* 361: 64–74.

35. Terada, N., Ohno, N., Li, Z., Fujii, Y., Baba, T. and Ohno, S. (2006) Application of in vivo cryotechnique to the examination of cell and tissues in living animal organs. *Histol. Histopathol.* 21: 265–272.

36. Terada, N., Saitoh, Y., Saitoh, S., Ohno, N., Jin, T. and Ohno, S. (2010) Visualization of microvascular blood flow in mouse kidney and spleen by quantum dot injection with "in vivo cryotechnique". *Microvasc. Res.* 80: 491–498.

37. Tiwari, D. K., Tanaka, S., Inouye, Y., Yoshizawa, K., Watanabe, T. M. and Jin, T. (2009) Synthesis and characterization of anti-HER2 antibody conjugated CdSe/CdZnS quantum dots for fluorescence imaging of breast cancer cells. *Sensors* 9: 9332–9364.

Contents lists available at ScienceDirect

Microvascular Research
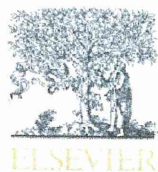
Imaging of thrombosis and microcirculation in mouse lungs of initial melanoma metastasis with in vivo cryotechnique

Yurika Saitoh [a], Nobuo Terada [a,b], Nobuhiko Ohno [a], Akiei Hamano [c], Nobuo Okumura [d], Takashi Jin [e], Ikuo Saiki [f], Shinichi Ohno [a,*]

[a] Department of Anatomy and Molecular Histology, Interdisciplinary Graduate School of Medicine and Engineering, University of Yamanashi, Chuo City, Yamanashi 409-3898, Japan
[b] Department of Occupational Therapy, School of Health Sciences, Shinshu University School of Medicine, Matsumoto City, Nagano 390-8621, Japan
[c] Central Research Laboratory of Nissui Pharmaceutical Co. Ltd., Yuuki City, Ibaraki 307-0036, Japan
[d] Department of Biomedical Laboratory Sciences, Laboratory of Clinical Chemistry, School of Health Sciences, Shinshu University School of Medicine, Matsumoto City, Nagano 390-8621, Japan
[e] Laboratory for Nano-Bio Probes, RIKEN Quantitative Biology Center, Suita City, Osaka 565-0874, Japan
[f] Division of Pathogenic Biochemistry, Institute of Natural Medicine, University of Toyama, Toyama City, Toyama 930-0194, Japan

ARTICLE INFO

ABSTRACT

Microscopic bioimaging of blood flow and distribution of cancer cells in lungs is essential to analyze mechanism of lung metastasis. Such cancer metastasis has been well known to induce hypercoagulable states and thrombosis. In histopathological tissue sections, however, it has been difficult to capture rapid phenomenon of thrombus formation due to technical problems associated with much less retention of soluble serum components as well as dynamic histological features reflecting their living states. In this study, to achieve bioimaging of both hypercoagulable states and thrombosis induced by early metastasis of mouse B16-BL6 melanoma, "in vivo cryotechnique" (IVCT) was used, which retained soluble components at their original sites. Glutathione-coated quantum dots (QDs) were subsequently injected after melanoma cells via right ventricles to examine plasma flow with fluorescence emission. At 5 s after the melanoma injection, melanoma cells were mostly stacked and intruded in alveolar capillaries with changing their shapes. Assembly of platelets initially appeared at 1 min, and they aggregated around the stacked melanoma cells at 5 min. Such aggregated platelets were immunopositive for both phospho-tyrosine 418 and 527 of Src, indicating their partial signal activation. Fibrin monomers were also immunolocalized around both melanoma cells and platelet aggregates, and massive immunoreaction deposits of fibrinogen were also detected near the same areas, but more strongly detected around the melanoma cells, indicating initial thrombus formation. In those areas, QDs were rarely detected, probably because of the lack of blood supply. Thus, IVCT revealed histopathological features of initial thrombosis under their circulatory conditions.

© 2013 Elsevier Inc. All rights reserved.

Introduction

It is well known that metastatic cancer cells easily induce hypercoagulable states including platelet aggregation, which are closely related to subsequent tumor progression, such as cell proliferation and angiogenesis (Hilgard, 1973; Holmes et al., 2009; Manegold et al., 2003). In addition to the platelets, some cancer cells were also demonstrated to produce coagulation factors, such as thrombin and tissue factors (Bambace and Holmes, 2011; Jain et al., 2010; Jurasz et al., 2004). Clinically, the hypercoagulable state of humans due to cancer progression often causes disseminated intravascular coagulation (DIC) (Bambace and Holmes, 2011; Kvolik et al., 2010). DIC is usually confirmed by blood and plasma tests of patients, indicating decreases of fibrinogen and platelet count, and/or increases of D-dimer, fibrinogen-degradation products and soluble fibrin monomer (Munter and Hershko, 2001). In particular, the level of soluble fibrin monomer is an indicator of initial blood coagulation because it is the first product of fibrinogen cleaved by thrombin (Budzynski et al., 1983). Such soluble fibrin monomers are also reported to enhance activated platelet adhesion to cancer cells, which was additionally confirmed by an increase of the lung metastasis of cancer cells pre-treated with soluble fibrin (Biggerstaff et al., 1999). To detect the soluble fibrin monomers in plasma in vitro, a monoclonal antibody was developed, which reacted to the conformation site of fibrinogen cleaved by thrombin (Hamano et al., 2002). However, for microscopic analyses of tissue sections, because most soluble components and molecular structures in blood vessels were readily removed or changed during tissue preparation with conventional chemical fixation methods, it has been difficult to use the antibody in addition to visualize

* Corresponding author at: Department of Anatomy and Molecular Histology, Interdisciplinary Graduate School of Medicine and Engineering, University of Yamanashi, 1110 Shimokato, Chuo City, Yamanashi 409-3898, Japan. Fax: +81 55 273 6743.
E-mail addresses: yurikas@yamanashi.ac.jp (Y. Saitoh), nobuot@shinshu-u.ac.jp (N. Terada), ohnoccf@gmail.com (N. Ohno), a-hamano@nissui-pharm.jp (A. Hamano), nobuoku@shinshu-u.ac.jp (N. Okumura), tjin@riken.jp (T. Jin), byosei@inm.u-toyama.ac.jp (I. Saiki), sohno@yamanashi.ac.jp (S. Ohno).

such functional areas and evaluate the timing of initial thrombus formation in conventionally prepared tissue sections.

"In vivo cryotechnique" (IVCT) has been very useful for the retention of soluble components of animal cells and tissues as well as molecular structures such as phosphorylation, as reported previously (Ohno et al., 1996, 2005; Saitoh et al., 2010; Shi et al., 2011; Terada et al., 2009). It makes it possible to analyze precisely the blood circulation conditions reflecting the living state in paraffin-embedded tissue sections. We recently applied it to living mouse lungs under normal and pulmonary hypertension conditions to examine the histopathological features (Saitoh et al., 2012). In such an experiment, three-dimensional reconstructed images of blood vessels and dynamic circulation were clearly demonstrated by the combination of IVCT and quantum dot (QD) injection on the order of seconds. In this report, we have presented tissue samples of initial melanoma metastasis in living mouse lungs with IVCT, revealing dynamic localizations of platelets with the activation of signal transduction of Src, some coagulation factors including fibrin monomers, and cancer cells under pathological blood circulation conditions using both immunostaining and QD injection in lung tissue sections reflecting their living states.

Materials and methods

Animals

All experimental procedures were in accordance with the Guidelines for Care and Use of Experimental Animals of the University of Yamanashi. Male 6- to 10-week-old C57BL/6J mice, weighing 18–25 g, were used in the present study. All mice were anesthetized by intraperitoneal administration of pentobarbital sodium (100 mg/kg body weight; Nakalai Tesque, Kyoto, Japan).

Melanoma cell culture

Mouse B16-BL6 melanoma cells were kindly provided by Dr. I. J. Fidler (Anderson Cancer Center, Houston, TX, USA). They were maintained as monolayer cultures in Eagle's MEM (EMEM; Sigma Aldrich Japan, Tokyo, Japan) supplemented with 10% fetal bovine serum (FBS). The cultures were kept at 37 °C in a humidified atmosphere of 5% CO_2/95% air.

IVCT for living mouse lungs and freeze-substitution fixation (FS)

IVCT was performed for living mouse lungs in a similar way to that previously reported (Saitoh et al., 2012). Briefly, mouse trachea was surgically exposed and connected to a small animal ventilator (SN-480-7; Shinano Manufacturing Co. Ltd., Tokyo, Japan). The respiratory rate was once a second, as reported previously (Saitoh et al., 2012; Terada et al., 2010). IVCT was performed by directly pouring liquid isopentane–propane (IP) cryogen (−193 °C) precooled with liquid nitrogen (LN_2; −196 °C) over the right lungs of anesthetized mice after injections of melanoma cells and/or subsequent QDs into their right ventricles, as described in the next paragraph.

The frozen lungs were removed with a dental electric drill in LN_2, and then processed for FS with acetone containing 2% paraformaldehyde at about −80 °C for 24 h. Then, the temperature of the frozen tissues was gradually increased to room temperature, as described previously (Saitoh et al., 2010). Finally, the freeze-substituted lungs were routinely embedded in paraffin wax.

Injection of B16-BL6 melanoma cells and QDs

To produce melanoma-injected mice, B16-BL6 melanoma cells suspended in phosphate-buffered saline (PBS) were directly injected into the right ventricles of their hearts (1×10^6 cells/100 μl/mouse). The melanoma cells were not aggregated before the injection, confirmed under a light microscope. For control mice, PBS alone with the same volume was injected into the right ventricles (100 μl/mouse). Then, at 1, 5 or 10 min after the melanoma injection, glutathione (GSH)-coated QDs, which always emitted 650 nm-wavelength fluorescent signals under ultraviolet (UV) light (Jin et al., 2008; Terada et al., 2010; Tiwari and Snure, 2008), were continuously injected into the right ventricles (10 μl/s). Then, IVCT was performed for the identical mouse lungs at 10 s after the QD injection (100 μl/mouse). To confirm the timing of the QD injection into lungs, IVCT was performed at 10 s after the continuous QD injection. The IVCT was also performed at 5 s after the continuous injection of melanoma cells (10 μl/s) alone to examine the timing of the melanoma injection into lungs.

To confirm this reproducibility, a total of 24 mice were used into the aforementioned eight experimental groups by using 3 mice each, (1) three groups for the QD injection at 1, 5 or 10 min after the melanoma cell injection; (2) three groups for the QD injection at 1, 5 or 10 min after the PBS injection; (3) one group for the continuous injection of melanoma cells alone for 5 s; and (4) one group for the continuous injection of QD alone for 10 s.

Various immunohistochemical stainings and QD detection by light microscopy

Paraffin-embedded specimens were serially cut into sections of 4 μm thickness, and mounted on NH_3^+-coated glass slides (MAS-GP™; Matsunami Glass Ind., Ltd., Osaka, Japan). The serial sections were routinely deparaffinized, and subjected to hematoxylin–eosin (HE) staining and immunostaining, or observed for QDs by fluorescence microscopy. Briefly, for the QD observation, deparaffinized slices with xylene were mounted with Multi Mount 220® (Matsunami Glass). The QD signal was detected by UV excitation in a fluorescence microscope (BX61; Olympus, Tokyo, Japan), as previously reported (Saitoh et al., 2012; Terada et al., 2010).

For immunostaining, some deparaffinized sections were treated with 0.3% hydrogen peroxide in PBS (pH 7.4) for 1 h, followed by 5% gelatin or normal goat serum in PBS for 1 h. Primary antibodies used for this study were as follows: goat polyclonal anti-mouse albumin antibody (Bethyl Lab. Inc., Montgomery, TX, USA), rabbit polyclonal anti-fibrinogen antibody (Dako Japan, Kyoto, Japan), biotin-labeled mouse monoclonal anti-soluble fibrin (F405) antibody (Hamano et al., 2002), rat monoclonal anti-CD42c antibody (EMFRET Analytics GmbH & Co., Würzburg, Germany), rabbit monoclonal anti-Src antibody (Cell Signaling Technology Japan, Tokyo, Japan), rabbit polyclonal anti-phospho-Src (Tyr418) antibody (Merck Millipore, Merck Ltd., Tokyo, Japan) and anti-phospho-Src (Tyr527) antibody (Cell Signaling Technology Japan). For immunostaining of soluble fibrin and phospho-Src (Tyr 527), deparaffinized sections were microwaved in 10 mM citrate buffer (pH 6.5) for antigen retrieval before the hydrogen peroxide treatment. For secondary antibodies, biotin-labeled rabbit anti-goat (Bethyl) IgG, goat anti-rabbit (Bethy) IgG or goat anti-rat IgG antibody (Jackson ImmunoResearch Lab. Inc., West Grove, PA, USA) was used. For the biotin-labeled antibodies, they were visualized by treatment with horseradish peroxidase (HRP)–avidin–biotin complex and followed by diaminobenzidine (ABC-DAB) (Thermo Fisher Scientific Inc., USA). Finally, they were observed under a light microscope (BX-61; Olympus).

For immunofluorescence staining, Alexa Fluor-594-conjugated goat anti-rat antibody (Life Technologies Japan Co. Ltd., Tokyo, Japan) or Alexa Fluor-488-conjugated goat anti-rabbit antibody (Life Technologies) was used as the secondary antibody. Then, immunostained sections were mounted in mounting medium with DAPI (Vector Laboratories, Inc., Burlingame, CA, USA). To detect the fluorescent signal, the immunostained sections were observed under a confocal laser scanning microscope (Olympus). To observe morphological structures, some sections were washed in PBS and distilled water, and routinely stained with HE, after immunofluorescence staining and subsequent detection of the fluorescent signal.

Quantitative measurement and statistical analysis

To evaluate how amount of melanoma cells intruded into alveolar capillaries, the ratio of the number of melanoma cells in alveolar capillaries to that of total melanoma cells was calculated within a total area of 25 mm² in 4 sections in 3 mice each. To evaluate septal locations of melanoma cells in large blood vessels, another ratio of the number of large blood vessels including melanoma cells to that of total large blood vessels was additionally calculated within a total area of 25 mm² in 4 sections in 3 mice each.

To examine the effects of melanoma cells on the aggregation of platelets, areas of CD42c-immunostained platelets were measured as pixels with Photoshop (Adobe systems Inc., San Jose, CA, USA). Then, they were converted into actual areas. The total numbers of areas in tissues at 1 and 5 min after PBS injection were 490 and 500 in 46 and 35 areas, respectively. Moreover, the numbers of areas in tissues at 1 and 5 min after the melanoma cell injection were 698 and 436 in 70 and 60 areas, respectively. Differences were analyzed with the Mann–Whitney U test, and the significance level was adjusted with the Bonferroni–Dunn test.

Results

Morphological features of early arrival of melanoma cells in lungs by IVCT

By IVCT, time-dependent images of experimental lung metastasis at various time intervals were precisely obtained on the order of seconds after the injection of melanoma cells. At 5 s, their initial entry into lung blood vessels was clearly detected, especially in large blood vessels and parts of alveolar capillaries (Figs. 1a–c). Some of them were filled with many flowing erythrocytes (white arrows in Figs. 1a–c). In addition, some melanoma cells elongated to pass through thinner alveolar capillaries (black arrowheads in Figs. 1d–g), indicating their capability to enter such dynamically changing alveolar capillaries from right ventricles within a few seconds.

Morphological features of melanoma cells including thrombosis and blood circulation with QD distribution

Next, to reveal the formation timing and histological imaging of thrombosis including platelets and melanoma cells, IVCT was performed on the order of minutes after their injection. At 1 min, some melanoma cells were stacked in alveolar capillaries (black arrowheads in Figs. 2a, d), and others were attached to endothelial walls of large blood vessels (black arrowheads in Figs. 2b, e), where erythrocytes appeared to be just entering. In several alveolar capillaries, some platelets got stacked (white arrowhead in Fig. 2f), suggesting the initiation of platelet aggregation within 1 min after the melanoma cell injection.

To demonstrate dynamic plasma flow in the presence of melanoma cells, QDs were continuously injected from right ventricles for 10 s, and then IVCT was performed in a similar way. Previously, we demonstrated that the GSH-QDs were rarely distributed in the interstitium in living mouse tissues in short-term experiments after its injection via hearts (Terada et al., 2010). In our recent study (Saitoh et al., 2012), QDs were clearly detected in lung venules at 2 s in an initial circulation area of living mouse lungs after the continuous injection of QDs, which were later detected in all blood vessels at 10 s. In this study, at 1 min after the melanoma cell injection, QDs were detected in all blood vessels as expected (Fig. 2g), localized in all blood vessels around the melanoma cells. Although some platelets started accumulating in a few blood vessels (inset in Fig. 2f), functional maintenance of blood circulation was definitely confirmed by QD localization at 1 min after the melanoma cell injection.

At 5 min after the melanoma cell injection, variously formed states of thrombosis appeared in many large blood vessels of living mouse lungs (Figs. 3a–k). In some blood vessels, melanoma cells were accompanied by larger aggregates of platelets (white arrowheads in Figs. 3f, g) with congested erythrocytes (black double-arrowheads in Figs. 3f, h). In some areas, many platelets also accumulated (white arrowheads in Fig. 3i) and aggregated in larger blood vessels (white double-arrowheads in Figs. 3i, j). The congested erythrocytes were
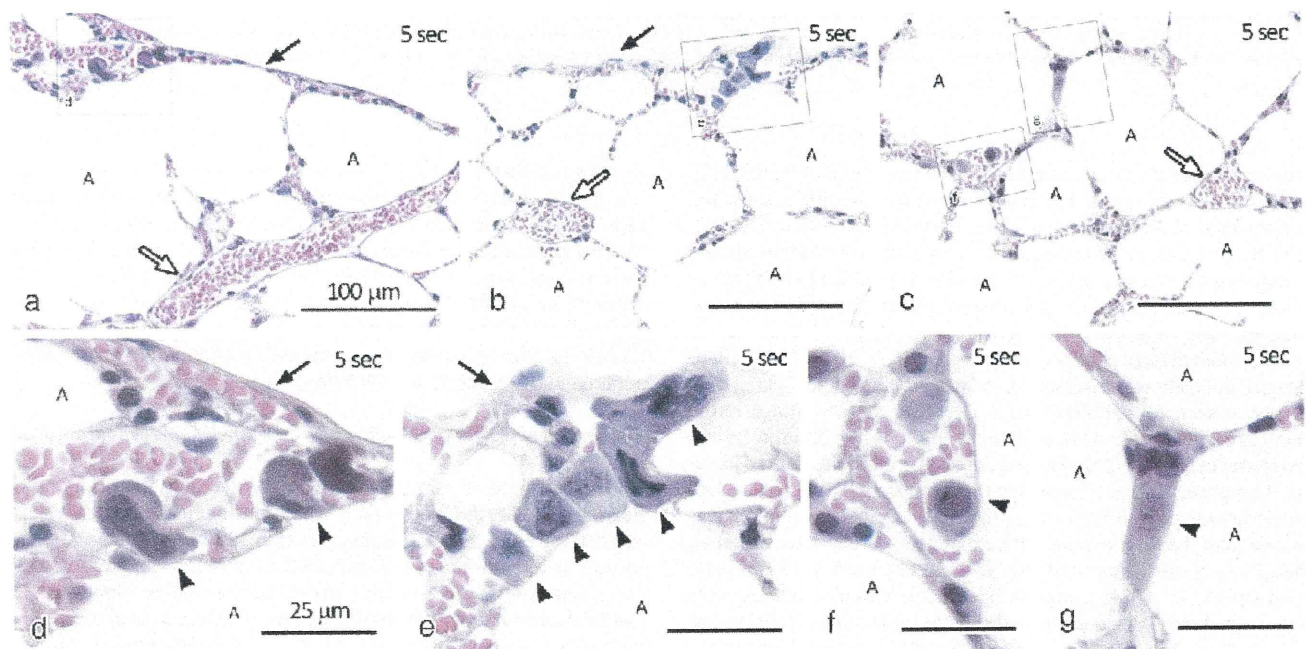

Fig. 1. Light micrographs of living mouse lung tissues prepared by IVCT at 5 s after the melanoma cell injection, which were obtained by HE staining. (a–c) In various tissue areas, melanoma cells are localized within blood vessels. (d–g) Highly magnified views of the boxed areas in (a–c). Black arrows in (a, b, d, e) indicate visceral pleura of lungs. Some melanoma cells often intrude in alveolar capillaries with alteration of their cellular shapes (black arrowheads in d, e). Other melanoma cells flowing in large blood vessels appear to be round (black arrowhead in f). A melanoma cell alone is clogging an alveolar capillary (black arrowheads in g). Blood vessels without melanoma cells are filled with many erythrocytes (white arrows in a–c). A: air space. Bars: 100 µm in (a–c), 25 µm in (d–g).
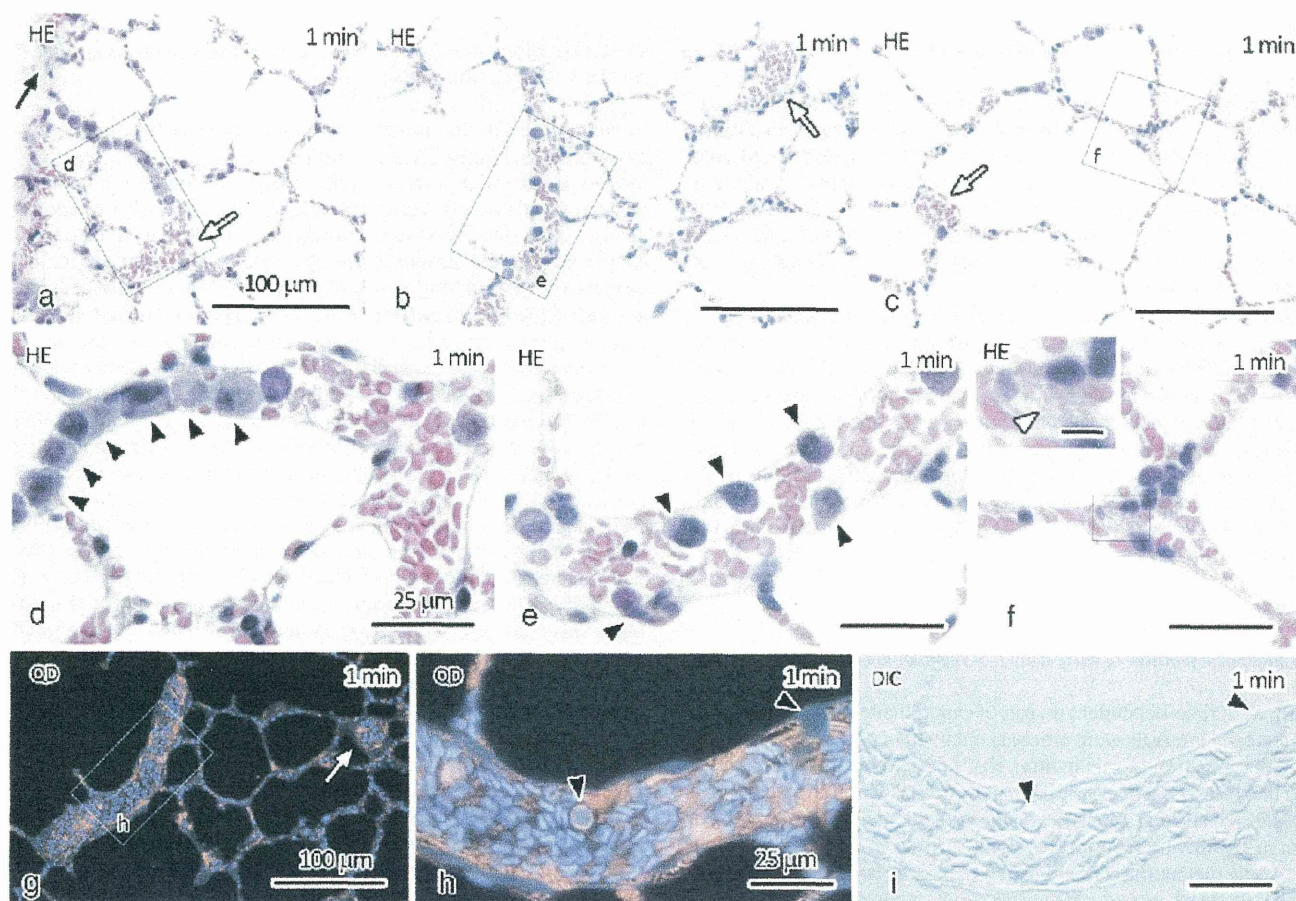
Fig. 2. HE-stained morphological features (HE; a–f) and distributions of QDs (QD; g, h) in living mouse lungs by IVCT at 1 min after the melanoma cell injection. Images of (d–f), inset of (f), and (h) are highly magnified views of the boxed areas in (a–c), (f), and (g), respectively. The section showing the red QD-fluorescence images with ultraviolet light (QD; g, h) and differential interference contrast images (DIC; i) is next to the serial paraffin section showing the HE-stained image (a, b, d, e). A black arrow in (a) indicates visceral pleura. The blood vessels (white arrows in a–c) and alveolar capillaries are all filled with variously shaped flowing erythrocytes. Some melanoma cells with large nuclei are stacked in blood vessels and also attached to endothelium of blood vessels (black arrowheads in d, e). Many platelets are loosely gathered in parts of blood vessels (white arrowhead in the inset of f). The injected QDs are distributed in all blood vessels (g, h) without (white arrow in g) or with melanoma cells (black arrowheads in h). Bars: 100 μm in (a–c, g), 25 μm in (d–f, h, i), 5 μm in inset of (f).

disproportionately located in such large blood vessels, and some faintly eosin-stained areas within blood vessels morphologically implied the maintenance of plasma flow with ice crystals (asterisk in Fig. 3k). Thus, the initial molecular structures of thrombus formation usually accompanied by melanoma cell metastasis were clearly visualized in HE-stained paraffin sections, reflecting the living state of mouse lungs. However, QDs were rarely detected in other areas of blood vessels, which contained large erythrocyte aggregates (Figs. 3l–n). The QD fluorescence intensity was inversely correlated to the platelet aggregation density, as seen in the differential interference contrast image. In the spotty areas, where flowing platelets were loosely gathered (white arrowhead in Fig. 3p), QDs were still detected around the stacked platelets. In contrast, in other areas where they compactly aggregated (white double-arrowheads in Figs. 3p, q), the QD fluorescence intensity was weaker than that in the areas where platelets were loosely gathered. Therefore, the distribution of QDs was not observed in 23% of large blood vessels (n = 748), suggesting that the vascular network was time-dependently occluded due to thrombus induced by the melanoma cell injection. These results suggest that IVCT revealed the initial morphology of thrombus formation, sometimes accompanied by later failure of blood circulation.

To statistically analyze the melanoma cells intruding into alveolar capillaries, we calculated the ratio of the number of melanoma cells in alveolar capillaries to that of total melanoma cells in paraffin sections (Fig. 3r). More than 50% of melanoma cells were intruding into alveolar capillaries at 1 and 5 min after the melanoma cell injection (Fig. 3r). However, the ratio of the number of large blood vessels including melanoma cells to that of total large blood vessels was not significantly different at any time point (Fig. 3s). These data suggest that some injected melanoma cells time-dependently intruded into alveolar capillaries, although other melanoma cells probably remained and/or adhered to the endothelial cells in large blood vessels.

Distribution of platelets in blood vessels under melanoma cell metastasis

To shed light on platelet aggregation, dynamic distributions of flowing platelets in blood vessels were immunohistochemically captured at the exact time of freezing. At 1 min after the melanoma cell injection, small deposits of stacked platelets immunostained for CD42c were detected as honeycomb patterns in some large blood vessels (white double-arrowheads in Figs. 4a, c–e), which contained melanoma cells (black arrowheads in Figs. 4c, d, f, g). Non-aggregated platelets were sparsely distributed in other alveolar capillaries (white arrowheads in Fig. 4b). At 5 min, total volumes of the platelet deposits increased in the large blood vessels (white double-arrowheads in Figs. 4h–n). In some of them, many melanoma cells were also detected
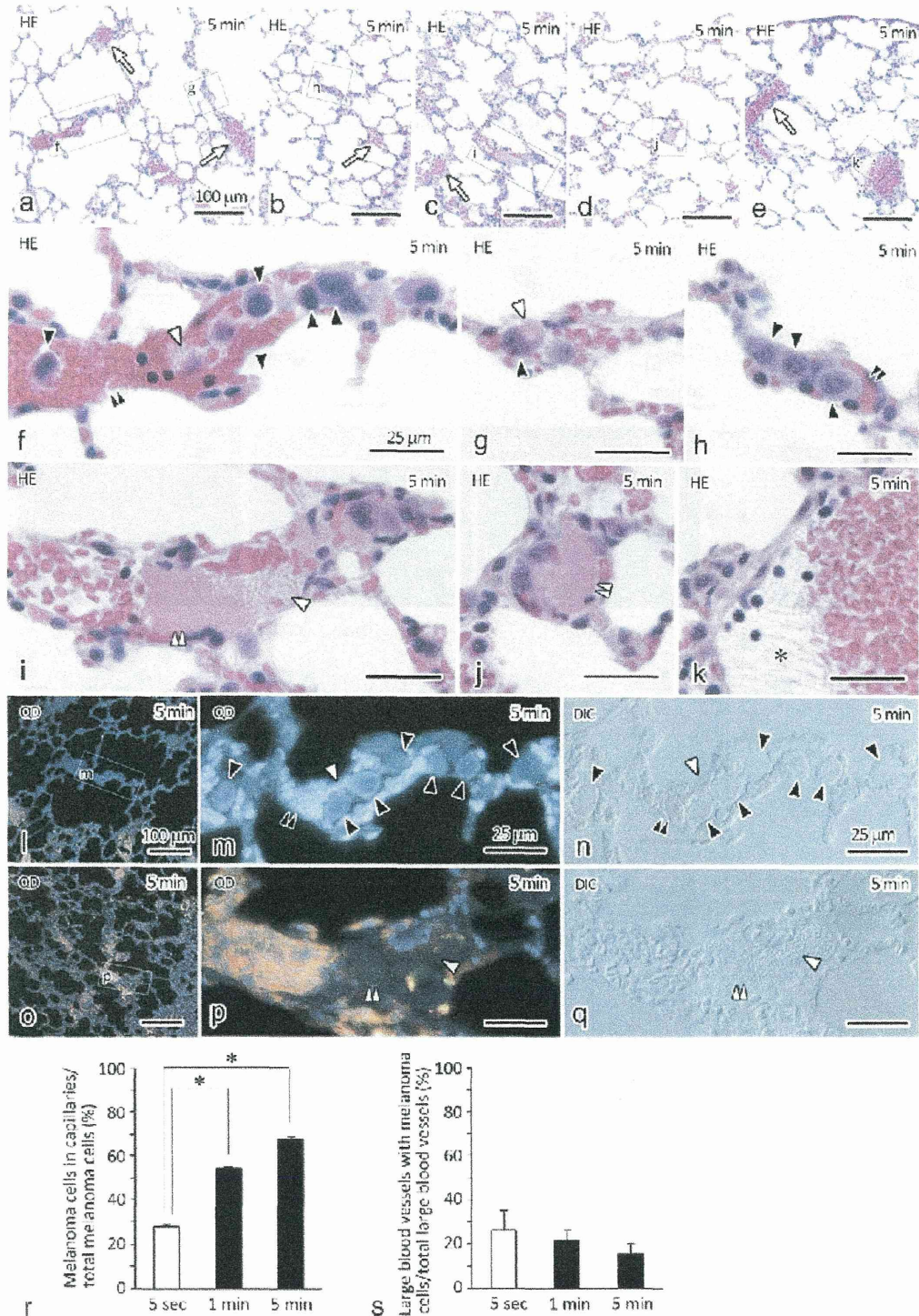
Fig. 3. HE-stained morphological features (HE; a–k) and distributions of QDs (QD; l, m, o, p) in living mouse lungs with IVCT at 5 min after the melanoma cell injection. Images of (f–k) and (m, n, p, q) are highly magnified views of the boxed areas in (a–e) and (l, o), respectively. Blood vessels (white arrows in a–c, e) are filled with many flowing erythrocytes. Melanoma cells with large nuclei are stacked in blood vessels and also attached to endothelium of blood vessels (black arrowheads in f–h). Some grouping platelets (white arrowheads in f, g, i) and many congested erythrocytes (black double-arrowheads in f, h) are localized in parts of blood vessels. In some blood vessels, large platelet aggregates occupy their lumens (white double-arrowheads in i, j). Plasma areas without flowing erythrocytes are identified with small ice crystals (asterisk in k). The red QD-fluorescence images with ultraviolet light (QD; l, m, o, p) and differential interference contrast images (DIC; n, q) are obtained in serial paraffin sections for the HE staining images (a, f, c, i). Large numbers of QDs are distributed in some areas of blood vessels (l, o). Images of (m) and (p) are highly magnified views of the boxed areas in (l) and (o), respectively. Flowing QD is rarely detected in the blood vessels that are filled with aggregated erythrocytes (black double-arrowheads in m), compact platelets (white arrowhead in m), and melanoma cells (black arrowheads in m). Such QD distributions appear to be mosaic-like patterns (o). The QD fluorescence intensity in some areas near the grouping platelets (white arrowhead in p) and also aggregated platelets (white double-arrowheads in p, q) is much weaker than that in the areas where erythrocytes have large space within blood vessels. (r) The ratio of the number of melanoma cells in alveolar capillaries to that of total melanoma cells, at 5 s (white column), 1 or 5 min (black column) after the melanoma cell injection. (s) The ratio of the number of large blood vessels including melanoma cells to that of total large blood vessels, at 5 s (white column), 1 or 5 min (black column). Bars: 100 μm in (a–e, l, o), 25 μm in (f–k, m, n, p, q). Asterisks: p < 0.01.